Qian Liu[1, 2], Yingjie Liu*[1], and Xiaofeng Li[1]

[1]CAS Key Laboratory of Ocean Circulation and Waves, Institute of Oceanology, Chinese Academy of Sciences, Qingdao 266071, China.

[2]University of Chinese Academy of Sciences, Beijing 100049, China.

*Email: yjliu@qdio.ac.cn.

Key Points:

- The main mechanism affecting eddy-induced pCO_2 depends on the strength of dissolved inorganic carbon within eddies.
- Eddy-induced pCO_2 is dominated by dissolved inorganic carbon (sea surface temperature) in winter (summer).
- About 1/4 of eddies in the Southern Ocean are abnormal (warm cyclonic and cold anticyclonic eddies) and have different effects on pCO_2.

Abstract

We investigate the role of mesoscale eddies in modulating the partial pressure of CO_2 (pCO_2) in the Southern Ocean from 1996 to 2015 using an eddy-centric composite method. The variation of pCO_2 is dominated by the balance between sea surface temperature (SST) and dissolved inorganic carbon (DIC) effects, which are affected by eddy-induced upwelling/downwelling. According to the rotation direction and SST signals, eddies can be classified into warm/cold and anticyclonic/cyclonic eddies and have different pCO_2 anomalies in different seasons. In winter, the pCO_2 anomalies within cold/warm eddies show positive/negative signals, which are dominated by DIC other than SST. However, in summer, the mechanisms affecting pCO_2 anomalies within eddies vary with regions in the Southern Ocean. In regions with larger (smaller) magnitudes of DIC anomalies, the pCO_2 anomalies within eddies are dominated by DIC (SST) anomalies and thus show positive/negative (negative/positive) signals within cold/warm eddies.

Plain Language Summary

Mesoscale eddies play a critical role in changing the dynamic ocean system in the Southern Ocean (SO). They profoundly impact biogeochemical cycling. This study investigates the characteristics of different types of mesoscale eddies in the SO. We analyzed the warm/cold anticyclonic eddies (WAEs/CAEs), warm/cold cyclonic (WCEs/CCEs) eddies, and their seasonal modulation on the partial pressure of CO_2 (pCO_2) in the SO from 1996 to 2015. The variation of pCO_2 differs in different eddies, influenced by the balance between dissolved inorganic carbon (DIC) and sea surface temperature (SST) effects. In winter, the pCO_2 anomalies are positive (negative) in CCEs and CAEs (WAEs and WCEs) dominated by DIC. However, in summer, the pCO_2 anomalies vary in different

regions of the SO, caused by the different magnitudes of DIC anomalies. In regions with larger (smaller) magnitudes of DIC anomalies, the pCO_2 anomalies are dominated by DIC (SST) anomalies and thus show positive/negative (negative/positive) signals within cold/warm eddies. Therefore, it is necessary to subdivide the types of eddies when investigating the eddy-induced modifications to pCO_2 or other oceanic variables.

1 Introduction

The sea surface partial pressure of CO_2 (pCO_2) dominates the variability in the air-sea flux of CO_2 (Lovenduski et al., 2008; McKinley et al., 2004; Takahashi et al., 2002). Thus, understanding pCO_2 variability is critical to quantifying the CO_2 absorption capacity of the ocean (Landschützer et al., 2015; McKinley et al., 2011; McKinley et al., 2017). The pCO_2 is primarily governed by sea surface temperature (SST) and dissolved inorganic carbon (DIC), and they are positively correlated (Chen et al., 2007; Iida et al., 2021; Jersild & Ito, 2020; Landschützer et al., 2015; Song et al., 2016). Besides, the competing seasonal cycles of DIC and SST affect the seasonal variability of pCO_2 (Jersild & Ito, 2020; Jiang et al., 2014; Munro et al., 2015). For example, in summer, strong biological utilization of carbon causes the minimum surface DIC and pCO_2 (Fay et al., 2018; Jersild & Ito, 2020; Munro et al., 2015; Takahashi et al., 2009). On the contrary, the warm SST lowers the solubility and thus elevates pCO_2. In winter, pCO_2 increases due to the suppression of biological productivity and upwelling of deep waters with high concentrations of DIC (Fay et al., 2018; Jersild & Ito, 2020; Landschützer et al., 2015). However, cold SST leads to higher solubility and thus decreases pCO_2.

Mesoscale eddies also affect the pCO_2 by modulating DIC and SST (Frenger et al., 2013; Song et al., 2016). According to eddies' rotation direction, they are classified into cyclonic eddies (CEs) and anticyclonic eddies (AEs), associated with upwelling and downwelling events, respectively. Upwelling brings cold and nutrient-rich deep water to the nutrient-deprived surface, while downwelling forces warm surface water downwards and leads to reduced productivity as it extends the depth of the nutrient-limited layer. Correspondingly, eddy-induced SST anomalies are generally positive (negative) within AEs (CEs) (Chelton et al., 2007; Chelton et al., 2011b; Faghmous et al., 2015), contrary to their eddy-induced DIC anomalies (Frenger et al., 2013; Song et al., 2016). However, previous studies found that the seasonal variation of pCO_2 within the eddies varies in different regions. For example, in the Drake Passage between the Atlantic and Pacific sectors of the Southern Ocean (SO), Song et al. (2016) found that AEs/CEs have negative/positive pCO_2 anomalies in summer, contrary to that in winter. They suggested that pCO_2 within eddies is dominated by DIC (SST) in summer (winter). However, in the Georgia Basin, the Atlantic sector of the SO, Jones et al. (2017) found that both AEs and CEs have negative pCO_2 anomalies dominated by DIC in summer. Within CEs, upwelled nutrient supply increased biological productivity, which counteracted DIC inputs from deep waters. This result is contrary to that reported by Song et al. (2016). In

other regions, researchers also found different effects of eddies on pCO_2 (Chen et al., 2007; Frenger et al., 2013). For instance, the pCO_2 in CEs increases in the subtropical North Pacific Gyre and decreases in the SO. These findings illustrate that the mechanisms of eddy-induced modifications to pCO_2 vary by season and region.

In addition, recent studies found that AEs can be further divided into warm anticyclonic eddies (WAEs) and cold anticyclonic eddies (CAEs), while CEs can be divided into cold cyclonic eddies (CCEs) and warm cyclonic eddies (WCEs) depending on SST (Leyba et al., 2017; Liu et al., 2020; Liu et al., 2021; Ni et al., 2021). Consequently, WAEs and CCEs are considered as normal eddies that obey conventional knowledge, and CAEs and WCEs are considered as abnormal ones. Abnormal eddies are ubiquitous in the ocean, accounting for about 32% of the total eddies in the global ocean (Liu et al., 2021). Moreover, the roles of abnormal eddies in ocean circulation (Shimizu et al., 2001), mass transportation (Everett et al., 2012; Mathis et al., 2007; Pickart et al., 2005), and air-sea interaction (Leyba et al., 2017; Liu et al., 2020) are different from normal ones (Assassi et al., 2016; Dilmahamod et al., 2018). Besides, Pezzi et al. (2021) found a WCE causing the ocean to act locally as a CO_2 source, contrary to the previous result that CCEs act locally as CO_2 sinks (Chen et al., 2007; Frenger et al., 2013; Jones et al., 2017). The case study preliminarily shows the difference between normal and abnormal eddies on pCO2, however, still lack of knowledge.

The study focuses on the characteristics of pCO_2 over normal and abnormal eddies in the SO. On the one hand, eddy activity is particularly strong in the SO (Frenger et al., 2015), and abnormal eddies in the Antarctic Circumpolar Current (ACC) region account for 19.9% of the total abnormal eddies in the global ocean (Liu et al., 2021). On the other hand, the absorption of anthropogenic CO_2 by the SO accounts for approximately 40% of the global ocean (Landschützer et al., 2015). Therefore, it is significant to comprehensively investigate the role of normal and abnormal eddies in regulating pCO_2 in the SO.

The study is organized as follows. First, section 2 presents data and the eddy-centric composite method. Then, in section 3, we illustrate the spatial distribution of eddy parameters for normal and abnormal eddies, present the seasonal variation of eddy-induced anomalies for pCO_2, DIC, and SST, and interpret the role of eddies in regulating the variability of pCO_2 in the SO. Finally, we conclude in section 4.

2 Data and Methods

2.1 SST, pCO_2, and DIC datasets

Three datasets of sea surface parameters are used in the study, including SST, pCO_2, and DIC from 1996 to 2015, between 30°S and 65°S. A brief description of each data is given below.

The daily SST dataset is the NOAA Optimum Interpolation (OI) SST product with 0.25° resolution, spanning from 1981 to the present (Reynolds et al., 2007). The OISST dataset combines observations from different platforms on a regular global grid, including Advanced Very High-Resolution Radiometer (AVHRR) satellite data, ships, buoys, and Argo floats with an accuracy of about 0.1 °C daily.

The pCO_2 and DIC datasets are from the JMA Ocean CO_2 Map dataset with monthly 1° × 1° gridded values on the global ocean from 1990 to 2020 (Iida et al., 2021). The DIC concentration is calculated from total alkalinity (TA) values and CO_2 fugacity (fCO_2) data in Surface Ocean CO_2 Atlas (SOCAT) (Bakker et al., 2016). The DIC field is estimated by using a multi-linear regression (MLR) method based on the DIC and satellite observation data, including SST, sea surface salinity (SSS), sea surface dynamic height (SSDH), chlorophyll (Chl), and surface mixed layer depth (MLD).

$$nDIC = f\,(time,\ SST,\ SSS,\ SSDH,\ Chl,\ MLD) \quad (1)$$

The pCO_2 field is then calculated from the fields of TA, DIC, SST, and SSS based on seawater CO_2 chemistry. The globally averaged error in DIC was 6.1 mol kg^{-1}, which is 5.4 mol kg^{-1} smaller than the error of GLODAPv2.2019. Moreover, the error in pCO_2 was 10.9 atm, comparable with those estimated with other empirical methods, e.g., 14.4 atm (Landschützer et al., 2014) and 15.73 atm (Denvil-Sommer et al., 2019). This dataset is widely used to study the relationship between pCO_2 and physical and biochemical parameters such as biological productivity, heat, and typhoons (Pittman et al., 2022; Rodgers et al., 2020; Swierczek et al., 2021; Yasunaka et al., 2019; Yu et al., 2020)

2.2 Eddy Database

Normal and abnormal eddies were identified by a deep learning (DL) model based on the fusion of satellite SSH and SST data (Liu et al., 2021). Based on the U-Net framework (Falk et al., 2019; Ronneberger et al., 2015), the model combines HyperDense-Net (Dolz et al., 2019) to fuse SSH and SST data. The SSH data is from the Archiving, Validation, and Interpretation of Satellite Oceanographic (AVISO). The SST data refers to the NOAA OISST product (Reynolds et al., 2007). The eddy data set is a daily and 0.25° resolution, including the number, radius, amplitude, rotational speed, and eddy kinetic energy (EKE) in the global ocean from 1996 to 2015. Besides, the model extracts SSH anomaly (SSHA) features for determining eddy locations and extracts SST anomaly (SSTA) information to distinguish between normal and abnormal eddies. The dice loss (a cost function to calculate the difference between the predicted and true values) and accuracy of the model were about 14% and 94% when training with the ground truth data set. Due to the limitations of the resolution capability of the SSHA data (Ducet et al., 2000), eddies with amplitudes < 2 cm and radii < 35 km were discarded in this work.

2.3 Eddy-centric Composite Method

To extract the eddy-induced mesoscale features in sea surface variables, including pCO_2, DIC, and SST, we used temporal and spatial filters similar to those used in Villas Bôas et al. (2015). The temporal filter is a band-pass Butterworth window (Butterworth, 1930) applied to preserve the temporal signal between 7 and 90 days corresponding to the typical time scales of the eddies. The spatial filter is a moving average Hann window (Stearns & Ahmed, 1976) designed to contain spatial signals smaller than 600 km. This filter removes the large-scale variability unrelated to the mesoscale eddy influence. Finally, the spatial pattern of the eddy-induced anomalies in sea surface variables was estimated using composite maps. For each identified eddy with a radius of R, the eddy-induced anomalies were mapped onto the eddy-centric coordinate spanning 2R. The advantage of the eddy-centric composite method is that averaging over many eddies helps suppress noise and reveal persistent eddy structures (Melnichenko et al., 2017).

3 Results and Discussion

3.1 Spatial Distributions of Normal and Abnormal Eddies in the SO

From 1996 to 2015, an average of 1991 eddies were identified daily in the SO (65°S–30°S), with abnormal eddies accounting for 26.3%. Figures 1a, 1b, 1d, and 1e show the spatial distribution of eddy number, defined as the frequency of eddies occurrence in each $1° \times 1°$ latitude-longitude bin over the analyzed period 1996–2015. All eddies disappear in the regions shallower than 2000m and the area near the Antarctica (shown in gray in Figure 1) because the bottom topography constrains the generation of eddies, and satellite altimetric cannot measure sea level beneath sea ice (Frenger et al., 2015). Normal and abnormal eddies are concentrated in the strong currents regions, such as the ACC, Western Boundary Current (WBC), and Eastern Boundary Current (EBC) regions (the current positions are shown in Figure S1). Such results are consistent with those findings by Frenger et al. (2015), which did not distinguish between normal and abnormal eddies. The differences between AEs and CEs, i.e., the eddy polarity, are critical for eddy-induced physical and biochemical anomalies (McGillicuddy et al., 1998; Siegel et al., 2011). The most significant difference between the polarity distributions of normal and abnormal eddies is the dominance of WCEs in the south and southwest of Australia (SA and SWA) (Figures 1f and S2).

Despite the great difference in the occurrence distributions of four kinds of eddies, their amplitude distributions are similar. Besides, eddies with larger amplitude concentrated in the Brazil Malvinas Confluence (BMC), Agulhas Return Current (ARC), ACC, EAC, and LC regions (Figures 1g, 1h, 1j, and 1k). The spatial distributions of rotational speed and EKE correlate well with the eddy amplitude patterns (Figure S3). Moreover, the polarity dominance of amplitude shows that CCEs (WCEs) have larger amplitudes than WAEs (CAEs) (Figures 1i and 1l). This finding can be interpreted by the gradient wind effect of centrifugal force, which pushes fluid outward in rotating eddies (Gill, 1982), intensifying the low pressure at the centers of CEs and weakening the high pressure at the centers of AEs (Chelton et al., 2011b). In addition, one should

note that the amplitudes of abnormal eddies are smaller than their normal ones (Figure S4a), consistent with previous studies (Liu et al., 2020; Liu et al., 2021).

3.2 Eddy-induced Modifications to pCO_2 in the SO

Using the eddy-centric composite method, we investigated the seasonal variations of pCO_2 anomalies associated with normal and abnormal eddies in the SO (Figure 2). The seasonal variations of SST and DIC anomalies are also analyzed since they are proposed to be the dominant factors that affect pCO_2. Figures 2a–2d and 2m–2p show the composite SST anomalies within normal and abnormal eddies in winter and summer, respectively. There are no significant differences in the signals and spatial patterns of SST anomalies within the same kind of eddies in summer and winter. Composite SST anomalies over normal eddies show asymmetric monopole patterns, with positive (negative) extremums slightly shifting westward and poleward (equatorward) relative to the WAEs (CCEs) cores. On the one hand, the meridional and zonal phase shifts were proposed to be induced by the large-scale background SST gradient and horizontal advection within eddies (Hausmann & Czaja, 2012; Liu et al., 2020; Villas Bôas et al., 2015). On the other hand, the positive (negative) SST anomalies are dominated by vertical heat advection induced by downwelling (upwelling) associated with WAEs (CCEs) (Delcroix et al., 2019; Huang et al., 2017; McGillicuddy et al., 1998). In comparison, abnormal eddies also display monopole patterns but with opposite signals. Previous works found opposite SST anomalies within abnormal eddies are influenced by eddy-wind interaction, which cause anomalous Ekman upwelling (downwelling) of the upper ocean density surfaces inside CAEs (WCEs) (Everett et al., 2012; Gaube et al., 2015; McGillicuddy et al., 2007; McGillicuddy, 2015; Ni et al., 2021). In addition, abnormal eddies may also be induced by instability during the eddy decay stage, eddy horizontal entrainment (Sun et al., 2019), and warm/cold background water (Leyba et al., 2017). Besides, subsurface-intensified eddies with opposite surface signatures may also appear as abnormal eddies in remote sensing images (Assassi et al., 2016). The paper focuses on the impacts of SST changes on DIC and pCO_2 inside eddies, other than determining which mechanism influences SST signals within eddies.

Figures 2e–2h and 2q–2t show the composite DIC anomalies within normal and abnormal eddies in winter and summer, respectively. The composite DIC anomalies within the same kind of eddies are similar in summer and winter, except that the magnitudes of DIC anomalies within eddies are slightly higher in winter. Besides, composite DIC anomalies within normal and abnormal eddies show dipole patterns dominated by opposite signals. For normal eddies, WAEs are dominated by negative DIC anomalies, which mainly stem from the eddy-induced downwelling of surface low-DIC waters (Figures 2e and 2q); CCEs are dominated by positive DIC anomalies, which mainly stem from the eddy-induced upwelling of deep rich-DIC waters (Figures 2g and 2s). By contrast, abnormal eddies show similar dipole patterns dominated by opposite signals (Figures 2f, 2h, 2r, and 2t). Such a result indicates that the process that

changes the SST signal within eddies also affects their DIC anomalies. For example, the anomalous Ekman upwelling/downwelling caused by eddy-wind interaction within CAEs/WCEs increases the magnitudes of positive/negative DIC anomalies. Moreover, the smaller amplitude within abnormal eddies reflects the weaker eddy-induced downwelling/upwelling, decreasing the magnitudes of negative/positive DIC anomalies. Consequently, the mean DIC anomalies within one radius of CAEs (WCEs) are positive (negative), contrary to their normal ones (Tables S2 and S3).

Unlike SST and DIC anomalies within eddies similar in summer and winter, pCO_2 anomalies within eddies in winter are significantly different from summer (Figures 2i–2l and 2u–2x). In winter, the pCO_2 anomalies have similar patterns with DIC anomalies, dominant by positive signals within CAEs and CCEs and negative signals within WAEs and WCEs (Figures 2i–2l). To quantify the similarity of the patterns between the pCO_2 and DIC (SST) anomalies over eddies, we used the structural similarity index (SSIM) (Wang et al., 2004) (Text S1). The closer the SSIM value is to 1, the more similar the two patterns are. The SSIMs are positive between pCO_2 and DIC anomalies but negative between pCO_2 and SST anomalies. Besides, SSIMs between pCO_2 and DIC anomalies are larger (>0.9), suggesting that the DIC effect dominates signatures of pCO_2 anomalies within eddies in winter. However, the SSIMs are negative between pCO_2 and DIC anomalies but positive between pCO_2 and SST anomalies over eddies in summer (<0.5). The spatial patterns of pCO_2 anomalies within eddies differ from their SST and DIC anomalies, reflecting the concurrent effects of SST and DIC on pCO_2. Considering the differences in the distributions of abnormal eddies and amplitude, we focus on the energetic regions dominated by normal eddies (BMC and ARC) and less energetic regions dominated by abnormal eddies (SWA and SA). Figure 3 shows the anomalies of SST, DIC, and pCO_2 over normal eddies in the BMC and ARC and over abnormal eddies in the SWA and SA in summer.

The pCO_2 anomalies within the same kind of eddies are opposite in the BMC and the ARC (Figures 3a and 3b). In the BMC (Figure 3a), the pCO_2 anomalies in WAEs/CCEs are positive/negative and show positive (negative) SSIMs with SST (DIC) anomalies. However, in the ARC (Figure 3b), the pCO_2 anomalies in WAEs/CCEs are negative/positive and show negative (positive) SSIMs with SST (DIC) anomalies. The results indicate that pCO_2 within eddies is dominated by the SST (DIC) in the BMC (ARC). There is no significant difference in SST anomalies over eddies between the BMC and ARC. In contrast, the magnitudes of DIC anomalies in the BMC are significantly less than the ARC, which may be the reason for the large difference in pCO_2 over eddies in the two regions.

Similar findings can be seen for the abnormal eddies in the SWA and the SA (Figures 3c and 3d). The DIC anomalies within eddies in the SWA are weaker than in the SA, and the two regions show opposite signals of pCO_2 anomalies over eddies. In the SWA, the pCO_2 anomalies are negative/positive within

CAEs/WCEs, dominated by the SST-driven effect (Figure 3c). In the SA, however, the pCO_2 anomalies are positive/negative within CAEs/WCEs, dominated by the DIC-driven effect (Figure 3d). We also compare the pCO_2 anomalies over eddies in the above regions in winter (Figure S6). The patterns are consistent with those in the SO during winter. The pCO_2 anomalies over eddies are determined by the DIC anomalies, which are associated with higher magnitudes in winter than in summer. Such seasonal magnitudes variation of DIC anomalies are controlled by the complex coupling of processes, biological activity (production/remineralization), vertical mixing, and air-sea gas exchanges (Racapé et al., 2010). These findings further prove that the different patterns of pCO_2 anomalies in the SO during summer result from the different magnitudes of DIC anomalies in different regions.

To further quantify the relationship between the pCO_2 and DIC (SST) anomalies over eddies, the mean pCO_2 anomalies within one eddy radius are binned onto equal intervals of DIC (SST) anomalies in summer (Figure 4) and winter (Figure S7). Using the least squares estimation, the linear relationship between pCO_2 and DIC (SST) anomalies is clear. The couplings between pCO_2 and DIC (SST) anomalies are positive (negative) linear correlated in winter (Figure S7). However, in summer, there is a linear negative (positive) correlation between pCO_2 and DIC (SST) anomalies in the SO, BMC, and SWA regions (Figures 4a–d) and a strong linear positive (negative) correlation between pCO_2 and DIC (SST) anomalies in the ARC and SA regions (Figures 4e and 4f). Besides, correlations between pCO_2 and DIC anomalies are weaker (stronger) than correlations between pCO_2 and SST anomalies in the regions with the dominant effect of SST (DIC) on pCO_2. In the SO, the coupling strength, that is, the slope of regression lines, between pCO_2 and DIC (SST) anomalies in abnormal eddies is higher (lower) than that in normal eddies (Figures 4a and 4b). This finding indicates that per umol/kg (degree) change in DIC (SST) in abnormal eddies can cause a larger (smaller) change in pCO_2. The growth rate of the coupling strength for pCO_2 and DIC anomalies between the ARC and BMC regions is much greater than that for pCO_2 and SST anomalies between the ARC and BMC regions (Figures 4c and 4d). The same principle applies to abnormal eddies in the SWA and SA regions (Figures 4d and 4f).

These results further support the idea that the DIC-driven effect dominates the pCO_2 anomalies in winter. However, in summer, whether the pCO_2 anomalies are dominated by SST- or DIC-driven effect depends on the magnitudes of DIC anomalies. The magnitudes of DIC anomalies in the BMC and SWA regions are smaller than in the ARC and SA regions. Therefore, the pCO_2 anomalies are dominated by SST-driven and DIC-driven effects, respectively. The coupling coefficients for all variables are summarized in Tables S4 and S5.

4 Conclusions

Using the eddy-centric composite method, we investigated the effects of mesoscale eddies in modulating the variability of pCO_2, DIC, and SST in the SO from 1996 to 2015. Based on SSTA, AEs (CEs) can be further divided

into WAEs and CAEs (CCEs and WCEs), leading to different modifications to pCO_2. The eddy-induced modulation of pCO_2 has a marked seasonal variability determined by the balance of SST-driven and DIC-driven effects. In summer, the pCO_2 anomalies in the SO are caused by different magnitudes of DIC anomalies in different regions, which determine whether the pCO_2 anomalies are dominated by SST- or DIC-driven effects. In ARC and SA (BMC and SWA) regions with the larger (smaller) magnitudes of DIC anomalies, the pCO_2 anomalies are dominated by the DIC-driven (SST-driven) effect, leading to positive/negative (negative/positive) pCO_2 in cold/warm eddies. However, in winter, the DIC anomalies are strong in different regions of the SO. Therefore, the pCO_2 anomalies are positive (negative) in CCEs and CAEs (WAEs and WCEs) caused by the dominant DIC-driven effect.

This study systematically investigates normal and abnormal eddies characteristics and their modifications to pCO_2 in the SO. The results reveal that the variation of pCO_2 is influenced by the balance of DIC and SST anomalies in eddies. The current research commonly combines all the AEs or CEs and masks the presence of CAEs and WCEs with very different upper ocean properties. Given their abundance, we consider the role of abnormal eddies when investigating eddy-induced modulation in air-sea variables, which helps to more accurately estimate the impact of mesoscale eddies on the global carbon cycle.

Acknowledgments

This work was supported by the Qingdao National Laboratory for Marine Science and Technology, the special fund of Shandong province (No. 2022QNLM050301-2), the Natural Science Foundation of Shandong Province (ZR2020MD083), the National Natural Science Foundation of China (U2006211), the Strategic Priority Research Program of the Chinese Academy of Sciences (XDA19060101, and XDB42000000), Major scientific and technological innovation projects in Shandong Province (2019JZZY010102), and the CAS Program (Y9KY04101L).

Open Research

All data used in the analysis are available in public repositories. The OISST data can be downloaded from https://www.ncei.noaa.gov/data/sea-surface-temperature-optimum-interpolation/v2.1/access/avhrr/. The pCO_2 and DIC datasets can be downloaded from https://www.data.jma.go.jp/gmd/kaiyou/english/co2_flux/co2_flux_data_en.html. Normal and abnormal eddies datasets can be downloaded from https://figshare.com/s/3c3b03776d9862ac85bc for peer review only.

References

https://doi.org/10.1175/jpo-d-15-0122.1

https://doi.org/10.5194/essd-8-383-2016

https://doi.org/10.1016/j.pocean.2011.01.002

https://doi.org/10.1029/2007gl030812
https://doi.org/10.1029/2006gl028058
https://doi.org/https://doi.org/10.1029/2018JC014394
https://doi.org/10.5194/gmd-12-2091-2019
https://doi.org/https://doi.org/10.1029/2018JC013828
https://doi.org/10.1109/TMI.2018.2878669
https://doi.org/https://doi.org/10.1029/2000JC900063
https://doi.org/10.1029/2012gl053091
https://doi.org/10.1038/sdata.2015.28
https://doi.org/10.1038/s41592-018-0261-2
https://doi.org/10.5194/bg-15-3841-2018
https://doi.org/10.1038/ngeo1863
https://doi.org/10.1002/2015jc011047
https://doi.org/10.1175/jpo-d-14-0032.1
https://doi.org/10.1016/j.dsr.2012.08.005
https://doi.org/https://doi.org/10.1002/2017JC012915
https://doi.org/10.1007/s10872-020-00571-5
https://doi.org/10.1029/2020gb006644
https://doi.org/10.1175/jcli-d-12-00571.1
https://doi.org/10.1016/j.dsr2.2015.10.006
https://doi.org/10.1002/2014gb004853
https://doi.org/doi:10.1126/science.aab2620
https://doi.org/10.1007/s00382-016-3460-5
https://doi.org/10.1029/2019jc015470
https://doi.org/10.1029/2021gl094772
https://doi.org/10.1029/2007gb003139
https://doi.org/10.1029/2006jc003899
https://doi.org/10.1175/jpo-d-14-0221.1
https://doi.org/doi:10.1126/science.1136256
https://doi.org/10.1038/28367
https://doi.org/10.1146/annurev-marine-010816-060529

https://doi.org/10.1038/ngeo1193

https://doi.org/10.1029/2003gb002179

https://doi.org/10.1002/2016jc012420

https://doi.org/10.1016/j.dsr2.2014.12.014

https://doi.org/10.1175/jpo-d-21-0010.1

https://doi.org/10.1038/s41598-021-89985-9

https://doi.org/10.1016/j.dsr2.2005.10.009

https://doi.org/https://doi.org/10.1029/2021GB007121

https://doi.org/10.1111/j.1600-0889.2010.00504.x

https://doi.org/10.1175/2007jcli1824.1

https://doi.org/10.1175/jcli-d-19-1022.1

https://doi.org/https://doi.org/10.48550/arXiv.1505.04597

https://doi.org/https://doi.org/10.1029/2011GL047660

https://doi.org/10.1002/2016jc011714

https://doi.org/10.1109/TSMC.1976.4309433

https://www.mdpi.com/2072-4292/11/2/208

https://doi.org/https://doi.org/10.1029/2021JC017235

https://doi.org/https://doi.org/10.1016/S0967-0645(02)00003-6

https://doi.org/10.1016/j.dsr2.2008.12.009

https://doi.org/10.1002/2015gl063105

https://doi.org/10.1109/TIP.2003.819861

https://doi.org/https://doi.org/10.1016/j.dsr2.2019.104680

https://doi.org/https://doi.org/10.1029/2020JC016258

Assassi, C., Morel, Y., Vandermeirsch, F., Chaigneau, A., Pegliasco, C., Morrow, R., et al. (2016). An Index to Distinguish Surface- and Subsurface-Intensified Vortices from Surface Observations. *Journal of Physical Oceanography*, *46*(8), 2529-2552. Bakker, D. C. E., Pfeil, B., Landa, C. S., Metzl, N., O'Brien, K. M., Olsen, A., et al. (2016). A multi-decade record of high-quality fCO_2 data in version 3 of the Surface Ocean CO_2 Atlas (SOCAT). *Earth System Science Data*, *8*(2), 383-413. Butterworth, S. (1930). On the theory of filter amplifiers. *Wireless Engineer* 193-195. Chelton, D. B., Schlax, M. G., & Samelson, R. M. (2011b). Global observations of nonlinear mesoscale eddies. *Progress in Oceanography*, *91*(2), 167-216. Chelton, D. B., Schlax, M. G., Samelson, R. M., & de Szoeke, R. A. (2007). Global observations of large oceanic eddies.

Geophysical Research Letters, *34*(15). Chen, F., Cai, W.-J., Benitez-Nelson, C., & Wang, Y. (2007). Sea surface $p\mathrm{CO}_2$-SST relationships across a cold-core cyclonic eddy: Implications for understanding regional variability and air-sea gas exchange. *Geophysical Research Letters*, *34*(10). Delcroix, T., Chaigneau, A., Soviadan, D., Boutin, J., & Pegliasco, C. (2019). Eddy-Induced Salinity Changes in the Tropical Pacific. *Journal of Geophysical Research: Oceans*, *124*(1), 374-389. Denvil-Sommer, A., Gehlen, M., Vrac, M., & Mejia, C. (2019). LSCE-FFNN-v1: a two-step neural network model for the reconstruction of surface ocean $p\mathrm{CO}_2$ over the global ocean. *Geoscientific Model Development*, *12*(5), 2091-2105. Dilmahamod, A. F., Aguiar-González, B., Penven, P., Reason, C. J. C., De Ruijter, W. P. M., Malan, N., et al. (2018). SIDDIES Corridor: A Major East-West Pathway of Long-Lived Surface and Subsurface Eddies Crossing the Subtropical South Indian Ocean. *Journal of Geophysical Research: Oceans*, *123*(8), 5406-5425. Dolz, J., Gopinath, K., Yuan, J., Lombaert, H., Desrosiers, C., & Ben Ayed, I. (2019). HyperDense-Net: A Hyper-Densely Connected CNN for Multi-Modal Image Segmentation. *IEEE Transactions on Medical Imaging*, *38*(5), 1116-1126. Ducet, N., Le Traon, P. Y., & Reverdin, G. (2000). Global high-resolution mapping of ocean circulation from TOPEX/Poseidon and ERS-1 and -2. *Journal of Geophysical Research: Oceans*, *105*(C8), 19477-19498. Everett, J. D., Baird, M. E., Oke, P. R., & Suthers, I. M. (2012). An avenue of eddies: Quantifying the biophysical properties of mesoscale eddies in the Tasman Sea. *Geophysical Research Letters*, *39*(16). Faghmous, J. H., Frenger, I., Yao, Y., Warmka, R., Lindell, A., & Kumar, V. (2015). A daily global mesoscale ocean eddy dataset from satellite altimetry. *Scientific Data*, *2*(1), 150028. Falk, T., Mai, D., Bensch, R., Cicek, O., Abdulkadir, A., Marrakchi, Y., et al. (2019). U-Net: deep learning for cell counting, detection, and morphometry. *Nature Methods*, *16*(1), 67-70. Fay, A. R., Lovenduski, N. S., McKinley, G. A., Munro, D. R., Sweeney, C., Gray, A. R., et al. (2018). Utilizing the Drake Passage Time-series to understand variability and change in subpolar Southern Ocean $p\mathrm{CO}_2$. *Biogeosciences*, *15*(12), 3841-3855. Frenger, I., Gruber, N., Knutti, R., & Münnich, M. (2013). Imprint of Southern Ocean eddies on winds, clouds and rainfall. *Nature Geoscience*, *6*(8), 608-612. Frenger, I., Münnich, M., Gruber, N., & Knutti, R. (2015). Southern Ocean eddy phenomenology. *Journal of Geophysical Research: Oceans*, *120*(11), 7413-7449. Gaube, P., Chelton, D. B., Samelson, R. M., Schlax, M. G., & O'Neill, L. W. (2015). Satellite Observations of Mesoscale Eddy-Induced Ekman Pumping. *Journal of Physical Oceanography*, *45*(1), 104-132. Gill, A. E. (1982). Atmosphere-Ocean Dynamic. *International Geophysics Series*. Hausmann, U., & Czaja, A. (2012). The observed signature of mesoscale eddies in sea surface temperature and the associated heat transport [Article]. *Deep-Sea Research Part I-Oceanographic Research Papers 70*, 60-72. Huang, J., Xu, F., Zhou, K., Xiu, P., & Lin, Y. (2017). Temporal evolution of near-surface chlorophyll over cyclonic eddy lifecycles in the southeastern Pacific. *Journal of Geophysical Research: Oceans*, *122*(8), 6165-6179. Iida, Y., Takatani, Y., Kojima, A., & Ishii, M. (2021). Global trends of ocean CO_2 sink and ocean acidification: an observation-based reconstruction of surface ocean inorganic carbon variables. *Journal of Oceanography*, *77*(2), 323-358. Jersild,

A., & Ito, T. (2020). Physical and Biological Controls of the Drake Passage pCO_2 Variability. *Global Biogeochemical Cycles*, *34*(9). Jiang, C., Gille, S. T., Sprintall, J., & Sweeney, C. (2014). Drake Passage Oceanic pCO_2: Evaluating CMIP5 Coupled Carbon–Climate Models Using in situ Observations. *Journal of Climate*, *27*(1), 76-100. Jones, E. M., Hoppema, M., Strass, V., Hauck, J., Salt, L., Ossebaar, S., et al. (2017). Mesoscale features create hotspots of carbon uptake in the Antarctic Circumpolar Current. *Deep Sea Research Part II: Topical Studies in Oceanography*, *138*, 39-51. Landschützer, P., Gruber, N., Bakker, D. C. E., & Schuster, U. (2014). Recent variability of the global ocean carbon sink. *Global Biogeochemical Cycles*, *28*(9), 927-949. Landschützer, P., Gruber, N., Haumann, F. A., Rödenbeck, C., Bakker, D. C. E., Heuven, S. v., et al. (2015). The reinvigoration of the Southern Ocean carbon sink. *Science*, *349*(6253), 1221-1224. Leyba, I. M., Saraceno, M., & Solman, S. A. (2017). Air-sea heat fluxes associated to mesoscale eddies in the Southwestern Atlantic Ocean and their dependence on different regional conditions. *Climate Dynamics*, *49*(7-8), 2491-2501. Liu, Y., Yu, L., & Chen, G. (2020). Characterization of Sea Surface Temperature and Air-Sea Heat Flux Anomalies Associated With Mesoscale Eddies in the South China Sea. *Journal of Geophysical Research: Oceans*, *125*(4). Liu, Y., Zheng, Q., & Li, X. (2021). Characteristics of Global Ocean Abnormal Mesoscale Eddies Derived From the Fusion of Sea Surface Height and Temperature Data by Deep Learning. *Geophysical Research Letters*, *48*(17). Lovenduski, N. S., Gruber, N., & Doney, S. C. (2008). Toward a mechanistic understanding of the decadal trends in the Southern Ocean carbon sink. *Global Biogeochemical Cycles*, *22*(3). Mathis, J. T., Pickart, R. S., Hansell, D. A., Kadko, D., & Bates, N. R. (2007). Eddy transport of organic carbon and nutrients from the Chukchi Shelf: Impact on the upper halocline of the western Arctic Ocean. *Journal of Geophysical Research: Oceans*, *112*(C5). McGillicuddy, D. J. (2015). Formation of Intrathermocline Lenses by Eddy–Wind Interaction. *Journal of Physical Oceanography*, *45*(2), 606-612. McGillicuddy, D. J., Anderson, L. A., Bates, N. R., Bibby, T., Buesseler, K. O., Carlson, C. A., et al. (2007). Eddy/Wind Interactions Stimulate Extraordinary Mid-Ocean Plankton Blooms. *Science*, *316*(5827), 1021-1026. McGillicuddy, D. J., Robinson, A. R., Siegel, D. A., Jannasch, H. W., Johnson, R., Dickey, T. D., et al. (1998). Influence of mesoscale eddies on new production in the Sargasso Sea. *Nature*, *394*(6690), 263-266. McKinley, G. A., Fay, A. R., Lovenduski, N. S., & Pilcher, D. J. (2017). Natural Variability and Anthropogenic Trends in the Ocean Carbon Sink. *Annual Review of Marine Science*, *9*, 125-150. McKinley, G. A., Fay, A. R., Takahashi, T., & Metzl, N. (2011). Convergence of atmospheric and North Atlantic carbon dioxide trends on multidecadal timescales. *Nature Geoscience*, *4*(9), 606-610. McKinley, G. A., Follows, M. J., & Marshall, J. (2004). Mechanisms of air-sea CO_2 flux variability in the equatorial Pacific and the North Atlantic. *Global Biogeochemical Cycles*, *18*(2). Melnichenko, O., Amores, A., Maximenko, N., Hacker, P., & Potemra, J. (2017). Signature of mesoscale eddies in satellite sea surface salinity data. *Journal of Geophysical Research: Oceans*, *122*(2), 1416-1424. Munro, D. R., Lovenduski, N. S., Stephens, B. B., Newberger, T., Arrigo, K. R., Takahashi, T., et al. (2015). Estimates of net community production

in the Southern Ocean determined from time series observations (2002–2011) of nutrients, dissolved inorganic carbon, and surface ocean pCO_2 in Drake Passage. *Deep Sea Research Part II: Topical Studies in Oceanography*, *114*, 49-63. Ni, Q., Zhai, X., Jiang, X., & Chen, D. (2021). Abundant Cold Anticyclonic Eddies and Warm Cyclonic Eddies in the Global Ocean. *Journal of Physical Oceanography*, *51*(9), 2793-2806. Pezzi, L. P., de Souza, R. B., Santini, M. F., Miller, A. J., Carvalho, J. T., Parise, C. K., et al. (2021). Oceanic eddy-induced modifications to air–sea heat and CO_2 fluxes in the Brazil-Malvinas Confluence. *Scientific Reports*, *11*(1), 10648. Pickart, R. S., Weingartner, T. J., Pratt, L. J., Zimmermann, S., & Torres, D. J. (2005). Flow of winter-transformed Pacific water into the Western Arctic. *Deep Sea Research Part II: Topical Studies in Oceanography*, *52*(24-26), 3175-3198. Pittman, N. A., Strutton, P. G., Johnson, R., Matear, R. J., & Sutton, A. J. (2022). Relationships Between Air-Sea CO_2 Flux and New Production in the Equatorial Pacific. *Global Biogeochemical Cycles*, *36*(4), e2021GB007121. Racapé, V., Monaco, L., Metzl, N., & Pierre, C. (2010). Summer and winter distribution of fÂ13CDIC in surface waters of the South Indian Ocean [20°S-60°S]. *Tellus B: Chemical and Physical Meteorology*, *62*(5), 660-673. Reynolds, R. W., Smith, T. M., Liu, C., Chelton, D. B., Casey, K. S., & Schlax, M. G. (2007). Daily High-Resolution-Blended Analyses for Sea Surface Temperature. *Journal of Climate*, *20*(22), 5473-5496. Rodgers, K. B., Ishii, M., Frölicher, T. L., Schlunegger, S., Aumont, O., Toyama, K., et al. (2020). Coupling of Surface Ocean Heat and Carbon Perturbations over the Subtropical Cells under Twenty-First Century Climate Change. *Journal of Climate*, *33*(23), 10321-10338. Ronneberger, O., Fischer, P., & Brox, T. (2015). U-Net: Convolutional Networks for Biomedical Image Segmentation. *Medical Image Computing and Computer-Assisted Intervention – MICCAI 2015*, 234-241. Siegel, D. A., Peterson, P., McGillicuddy Jr., D. J., Maritorena, S., & Nelson, N. B. (2011). Bio-optical footprints created by mesoscale eddies in the Sargasso Sea. *Geophysical Research Letters*, *38*(13). Song, H., Marshall, J., Munro, D. R., Dutkiewicz, S., Sweeney, C., McGillicuddy, D. J., et al. (2016). Mesoscale modulation of air-sea CO_2 flux in Drake Passage. *Journal of Geophysical Research: Oceans*, *121*(9), 6635-6649. Stearns, S. D., & Ahmed, N. (1976). Digital Signal Analysis. *IEEE Transactions on Systems, Man, and Cybernetics*, *SMC-6*(10), 724-724. Sun, W., Dong, C., Tan, W., & He, Y. (2019). Statistical Characteristics of Cyclonic Warm-Core Eddies and Anticyclonic Cold-Core Eddies in the North Pacific Based on Remote Sensing Data. *Remote Sensing*, *11*(2), 208. Swierczek, S., Mazloff, M. R., Morzfeld, M., & Russell, J. L. (2021). The Effect of Resolution on Vertical Heat and Carbon Transports in a Regional Ocean Circulation Model of the Argentine Basin. *Journal of Geophysical Research: Oceans*, *126*(7), e2021JC017235. Takahashi, T., Sutherland, S. C., Sweeney, C., Poisson, A., Metzl, N., Tilbrook, B., et al. (2002). Global sea–air CO_2 flux based on climatological surface ocean pCO_2, and seasonal biological and temperature effects. *Deep Sea Research Part II: Topical Studies in Oceanography*, *49*(9), 1601-1622. Takahashi, T., Sutherland, S. C., Wanninkhof, R., Sweeney, C., Feely, R. A., Chipman, D. W., et al. (2009). Climatological mean and decadal change in surface ocean pCO_2, and net sea–air CO_2 flux over the global

oceans. *Deep Sea Research Part II: Topical Studies in Oceanography*, *56*(8-10), 554-577. Villas Bôas, A. B., Sato, O. T., Chaigneau, A., & Castelão, G. P. (2015). The signature of mesoscale eddies on the air-sea turbulent heat fluxes in the South Atlantic Ocean. *Geophysical Research Letters*, *42*(6), 1856-1862. Wang, Z., Bovik, A. C., Sheikh, H. R., & Simoncelli, E. P. (2004). Image quality assessment: from error visibility to structural similarity. *IEEE Transactions on Image Processing*, *13*(4), 600-612. Yasunaka, S., Kouketsu, S., Strutton, P. G., Sutton, A. J., Murata, A., Nakaoka, S., et al. (2019). Spatio-temporal variability of surface water pCO_2 and nutrients in the tropical Pacific from 1981 to 2015. *Deep Sea Research Part II: Topical Studies in Oceanography*, *169-170*, 104680. Yu, P., Wang, Z. A., Churchill, J., Zheng, M., Pan, J., Bai, Y., et al. (2020). Effects of Typhoons on Surface Seawater pCO_2 and Air-Sea CO_2 Fluxes in the Northern South China Sea. *Journal of Geophysical Research: Oceans*, *125*(8), e2020JC016258. Figure Legends

Figure 1. Spatial distribution of (a, b, d, and e) frequency, (g, h, j, and k) amplitude, and polarity dominance in the SO from 1996 to 2015. (c, f) Ratio of the area occupied by WAEs (CAEs) over the area covered by CCEs (WCEs). (i, l) Ratio of amplitude for WAEs (CAEs) over CCEs (WCEs). Black lines show the mean northern and southern positions of the ACC major fronts.

Figure 2. Eddy-centric composite averages for seasonal anomalies of SST, pCO_2, and DIC in the SO. On each map, a black dot denotes the eddy center, and a white dot denotes the center location of variables (defined by the location of the extremum value). Contour intervals are every 0.01 °C for SST, every 0.07 umol/kg for DIC, and every 0.02 uatm for pCO_2. The numbers in the lower right corner are the SSIM.

Figure 3. Eddy-centric composite averages for SST, DIC, and pCO_2 anomalies in the (a) BMC, (b) ARC, (c) SWA, and (d) SA regions in summer. On each map, a black dot denotes the eddy center, and a white dot denotes the center location of variables (defined by the location of the extremum value). Contour intervals are every 0.02 (0.008) °C for SST, every 0.13 (0.08) umol/kg for DIC, and every 0.05 (0.04) uatm for pCO_2 in BMC and ARC (SWA and SA) regions. The numbers in the lower right corner are the SSIM.

Figure 4. The mean pCO_2 averaged within one radius of different eddies as a function of the respective eddy SST and DIC in the (a, b) SO, (c) BMC, (d) SWA, (e) ARC, and (f) SA regions in summer. Different colors denote different anomalies associated with different eddies. Dots denote the values averaged at the binned SST (DIC) intervals of 0.02 °C (0.03 umol/kg) in the SO, BMC, and ARC regions and DIC intervals of 0.01 umol/kg in the SWA and SA regions. Solid lines denote the regression lines obtained from least squares fitting with S being the slope and R the correlation coefficient.

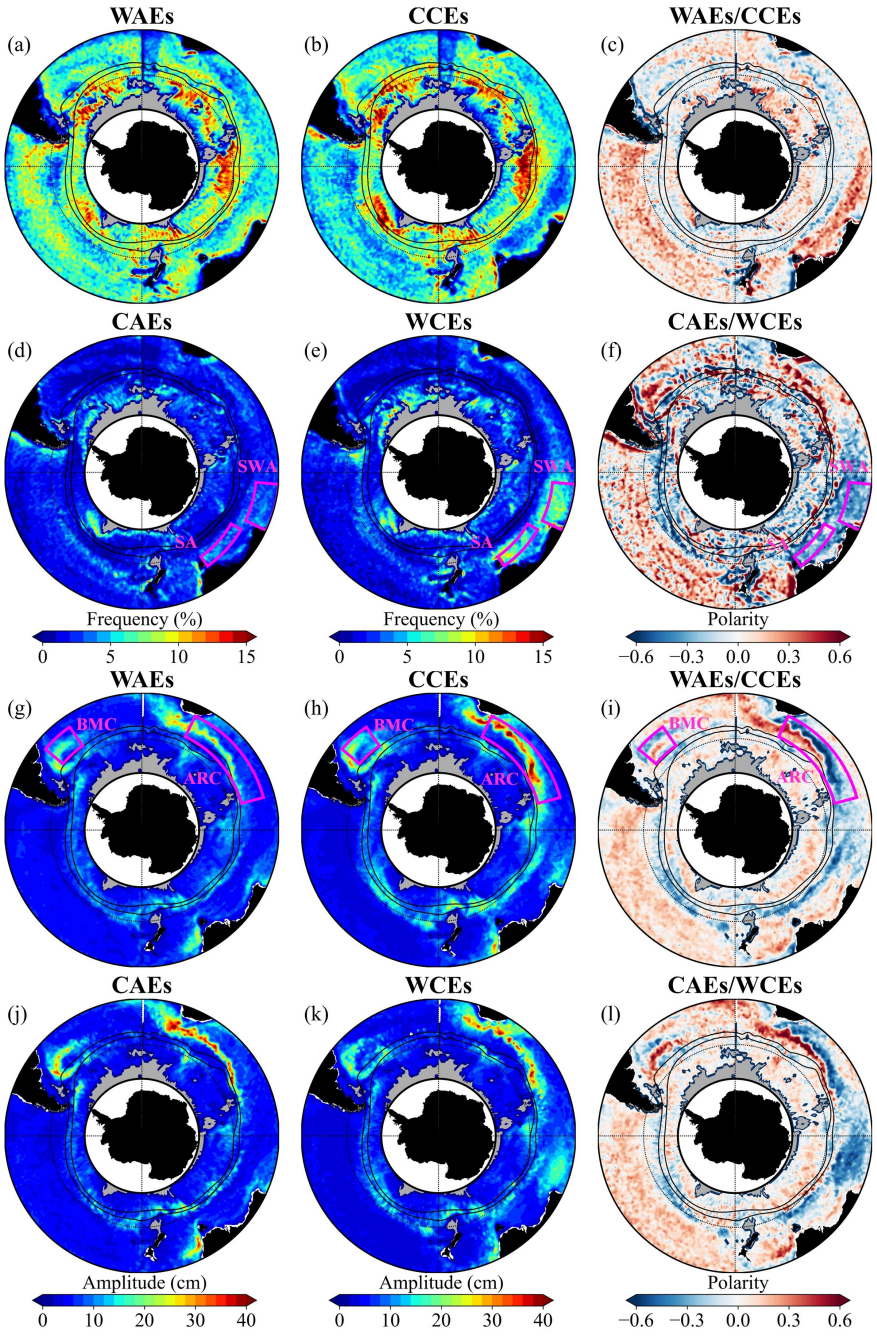

Figure 1. Spatial distribution of (a, b, d, and e) frequency, (g, h, j, and k) amplitude, and polarity dominance in the SO from 1996 to 2015. (c, f) Ratio of the area occupied by WAEs (CAEs) over the area

covered by CCEs (WCEs). (i, l) Ratio of amplitude for WAEs (CAEs) over CCEs (WCEs). Black lines show the mean northern and southern positions of the ACC major fronts.

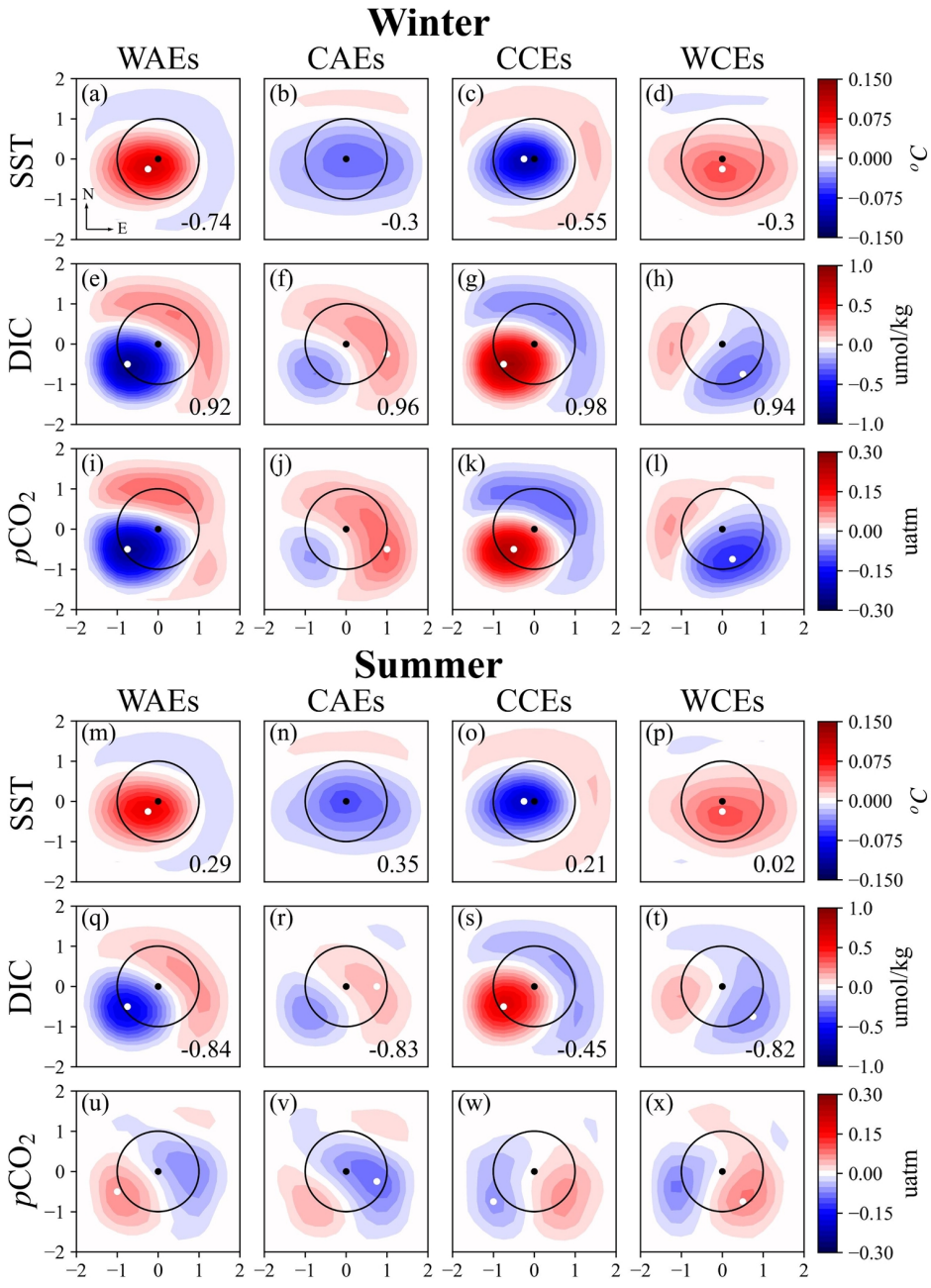

Figure 2. Eddy-centric composite averages for seasonal anomalies of

SST, pCO_2, and DIC in the SO. On each map, a black dot denotes the eddy center, and a white dot denotes the center location of variables (defined by the location of the extremum value). Contour intervals are every 0.01 °C for SST, every 0.07 umol/kg for DIC, and every 0.02 uatm for pCO_2. The numbers in the lower right corner are the SSIM.

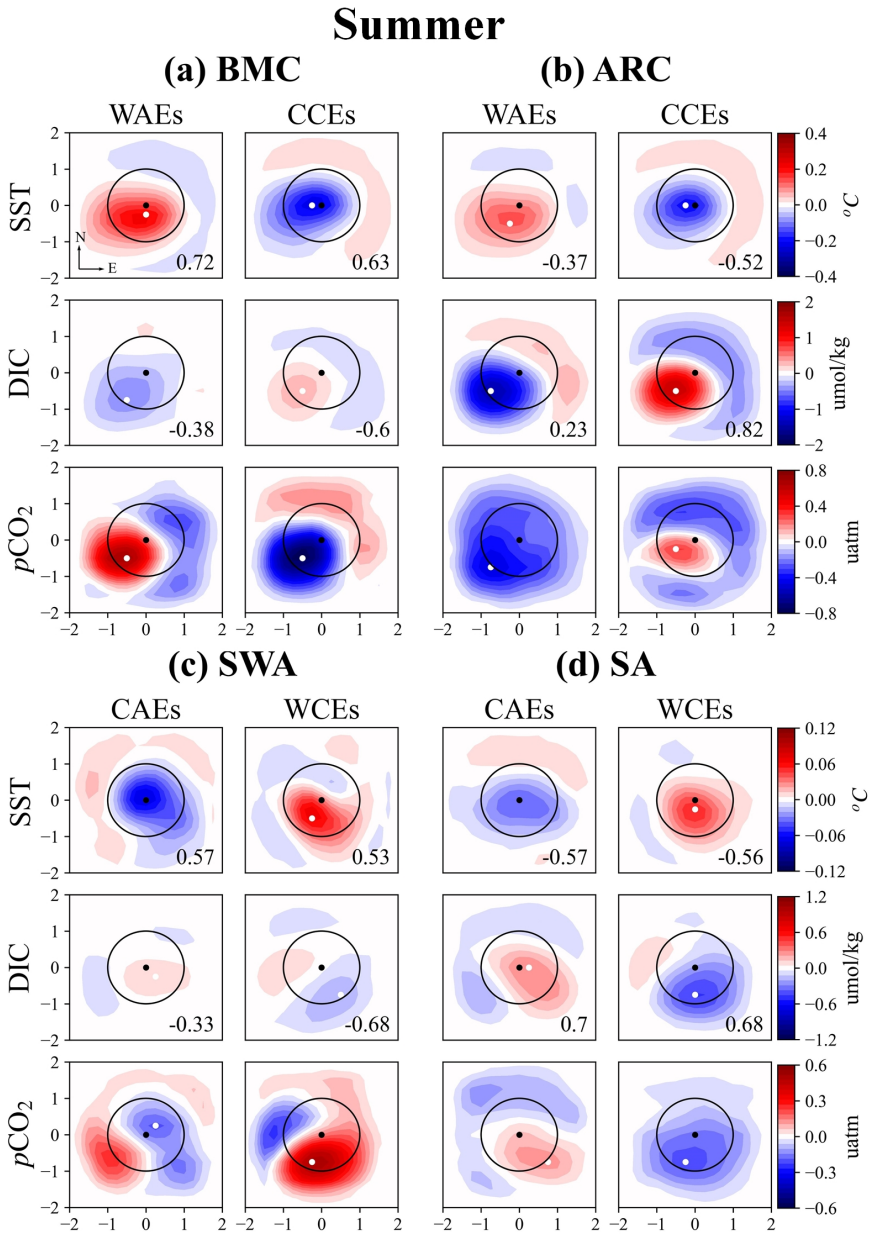

Figure 3. Eddy-centric composite averages for SST, DIC, and pCO_2 anomalies in the (a) BMC, (b) ARC, (c) SWA, and (d) SA regions in summer. On each map, a black dot denotes the eddy center, and a white dot denotes the center location of variables (defined by the location of the extremum value). Contour intervals are every 0.02 (0.008) °C for SST, every 0.13 (0.08) umol/kg for DIC, and every 0.05 (0.04) uatm for pCO_2in BMC and ARC (SWA and SA) regions. The numbers in the lower right corner are the SSIM.

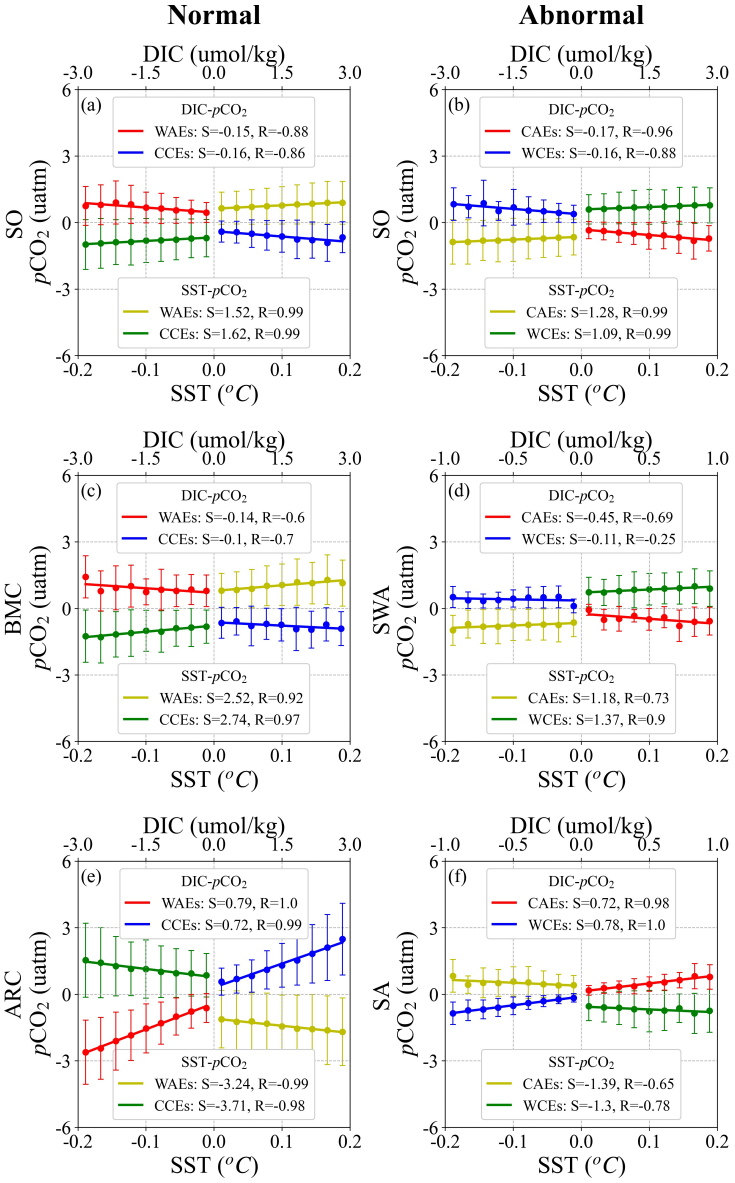

Figure 4. The mean pCO_2 averaged within one radius of different eddies as a function of the respective eddy SST and DIC in the (a, b) SO, (c) BMC, (d) SWA, (e) ARC, and (f) SA regions in summer. Different colors denote different anomalies associated with different eddies. Dots denote the values averaged at the binned SST (DIC) intervals of 0.02 °C (0.03 umol/kg) in the SO, BMC, and ARC regions and DIC intervals of 0.01 umol/kg in the SWA and SA regions. Solid lines denote the regression lines obtained from least squares fitting with S being the slope and R the correlation coefficient.